pubs.acs.org/Biomac

Article

Polymer Coatings on Virus-like Particle Nanoreactors at Low Ionic Strength—Charge Reversal and Substrate Access

Pawel Kraj, Ekaterina Selivanovitch, Byeongdu Lee, and Trevor Douglas*

Cite This: https://doi.org/10.1021/acs.biomac.1c00208

Read Online

ACCESS | Metrics & More | Article Recommendations | Supporting Information

ABSTRACT: Virus-like particles (VLPs) are a class of biomaterials which serve as platforms for achieving the desired functionality through interior and exterior modifications. Through ionic strength-mediated electrostatic interactions, VLPs have been assembled into hierarchically ordered materials. This work builds on predictive models to prepare polymer-coated VLP clusters at very low ionic strength. Zeta potential measurements showed that the clusters carried a strongly positive charge, a complete charge reversal from the VLP building block. SAXS analysis confirmed polymer adsorption onto the VLP exterior. We then studied the activity of an encapsulated enzyme toward small molecular and macromolecular substrates to determine the effect of each component of the hierarchically assembled material. We found that while encapsulation and polymer coating did not have a large effect on access to the enzyme by its native, small molecular substrate, substrate modification with a macromolecule caused the polymer coating and encapsulation to affect the access to the enzyme.

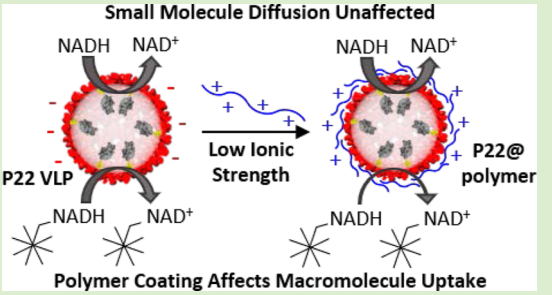

INTRODUCTION

Low solution ionic strength maximizes the effect of electrostatic interactions on materials. Because the Debye length — the distance over which a charge carrier's electrostatic effect persists in solution — increases exponentially as the ionic strength approaches zero, the effect of charge on materials under very low ionic strength conditions is more pronounced than under biologically relevant physiological ionic strength conditions. For example, the binding of negatively charged RNA to the positively charged active site of RNAseA is stronger at low ionic strength, leading to an increase in enzyme activity.[1] Similarly, fluorescent protein probes for reporting ionic strength are more responsive at low salt concentrations.[2] The increase of the polymer persistence length as a result of decreased charge screening has also been well studied.[3,4] However, despite the characterization of individual material behavior at low ionic strength, there has been little work done on hierarchically assembled enzyme materials in this region.

The deposition of a single layer of polymer on a surface is the first step in the formation of an LbL (layer-by-layer) assembly. LbL assemblies are thin films formed from the electrostatically driven step-by-step addition of oppositely charged macromolecules to a surface.[5] Each layer reverses the charge of the surface and is held on the previous layer through electrostatic interactions. The LbL architecture can use different macromolecules, including polymers and virus-like particles (VLPs), and can be deposited on a wide variety of surfaces including silicon slides, protein crystals, and colloidal nanoparticles.[5−9] LbL polymer structures have been used functionally to protect protein cargo from degradation or as supports for incorporation of sensor molecules.[7,10]

Protein cages such as VLPs are large, symmetrical macromolecules which assemble from many individual copies of identical protein subunits. Protein cages serve as an architecture for biological functions such as iron mineralization and storage and protection of genetic material.[11,12] In particular, VLPs are noninfectious protein cage nanoparticles assembled from capsid proteins and, where applicable, a scaffolding molecule such as a protein, polymer, or nanoparticle.[13−16] These assembled polyelectrolyte VLPs are useful platforms for diverse materials design because they can be functionalized on the interior, the exterior, or the interface between protein subunits, and can be incorporated into functional 3-D materials.[12,17] The range of functionality extends from modification with small molecules or polymers to encapsulation of enzymes and presentation of antigenic proteins.[18−21] In each case, the VLP serves as a platform for a material which derives functionality from the chosen modification.[22−24]

Bacteriophage P22 is an icosahedral $T = 7$ virus which infects *Salmonella typhimurium*. The infectious virus assembles

Received: February 15, 2021
Revised: April 7, 2021

into a spherical procapsid cage around a scaffolding protein from several structural proteins.[25] Procapsid VLPs derived from bacteriophage P22 self-assemble inside cells where just two proteins − the coat protein (CP) and the scaffold protein (SP) − are expressed.[14] A protein targeted for encapsulation within the VLP can be genetically fused to the scaffold protein, leading to the assembly of a VLP loaded with a protein cargo including catalytically active enzymes.[26] The porous nature of P22 allows access to encapsulated enzymes by small molecule substrates, but protects the interior cargo from degradation and allows for easy separation through centrifugation, making the VLPs a promising building block for catalytic materials.[27,28]

Functional VLPs and other protein cages can be incorporated into higher-order assemblies through electrostatic interactions with oppositely charged polymers and dendrimers.[29−32] Electrostatically driven self-assembly is mediated by the strength of the electrostatic interactions between cationic and anionic macromolecules, which is screened by ions in solution. This screening effect is described by the Debye length (κ^{-1}) and is modulated by controlling the ionic strength of the medium. At low ionic strengths, the interaction between negatively charged VLPs and cationic dendrimers is strong, leading to the kinetically driven formation of amorphous materials.[33] As the ionic strength increases, the assembly product is increasingly thermodynamically driven, leading to crystalline materials.[34] At a sufficiently high ionic strength, the threshold ionic strength (I_T), the formation of a material product abruptly stops due to screening of the attractive electrostatic interactions.[31,33] The ionic strength-dependent aggregation of P22 VLPs with G6 polyamidoamine (PAMAM) dendrimers has been computationally modeled with experimental validation of the simulation results.[35] At very low ionic strength, the interaction between the dendrimer and the VLPs is strong, causing the formation of a single layer of dendrimers around each capsid and preventing the formation of larger aggregates.

P22 VLPs carry high negative charge on their exterior surfaces and at their pores. These charges provide a support for the deposition of a polymer layer on the particle exterior. To better understand the effects of low ionic strength on P22 nanoreactors and their interactions with charged macromolecules and enzyme substrates, we investigated the interaction between P22 VLP nanoreactors and charged polymers, which, at low ionic strength, resulted in the adsorption of a layer of polymer on the VLP exterior. We hypothesized that the addition of the polymer layer would affect diffusion of charged substrates into the capsid through the introduction of electrostatic or steric factors. We show the charge reversal of P22 VLPs through the deposition of a cationic polymer layer, which could only be achieved at low ionic strength. The AdhD enzyme encapsulation in P22 is well established in our lab and its behavior is highly reproducible making it a good model system for probing the effects of substrate charge on diffusion through the outer layers (capsid and polymer), particularly at low ionic strength. The active AdhD enzyme is genetically fused to the scaffolding protein, and this facilitates both the P22 capsid assembly and the encapsulation of the AdhD on the interior of the capsid.[28] Through monitoring the activity of AdhD toward a charged substrate, we compared the behavior of the functional building block to the behavior of the enzyme encapsulated inside P22 VLPs as well as investigated the effect of polymer-coated VLPs on substrate access to the enzyme.

MATERIALS AND METHODS

Expression of P22-GFP. *E. Coli* BL21 cells were transformed with a pRSF-Duet vector containing genes encoding for wild-type P22 coat protein and GFP-scaffold protein fusion. Protein expression was induced through addition of IPTG to a final concentration of 1 mM when cells reached an early log growth phase (OD_{600} = 0.6). After 4 h, cells were harvested by centrifugation at 4500*g* for 10 min and stored at −80 °C for at least 2 h or until purification.

Expression of P22-AdhD. *E. Coli* BL21 cells were cotransformed with a pRSF-Duet vector encoding for the wild-type P22 coat protein and a pBAD vector encoding for AdhD-scaffold protein fusion. Cells were grown in LB media at 37 °C in the presence of kanamycin and ampicillin. Expression of AdhD-SP was induced through addition of arabinose to a final concentration of 13.3 mM when cells reached early log growth phase (OD_{600} = 0.6). After 4 h, expression of P22 coat protein was induced through addition of IPTG to a final concentration of 0.5 mM. Cells were grown overnight at room temperature and harvested by centrifugation at 4500*g* for 10 min and stored at −80 °C for at least 2 h or until purification.

Purification of P22 VLPs. Postexpression cell pellets were thawed, resuspended in lysis buffer (50 mM sodium phosphate, 100 mM sodium chloride, pH 7.2), and incubated with DNAse, RNAse, and lysozyme for 45 min at room temperature. The cell suspension was lysed by sonication and then centrifuged at 12,000 rpm for 45 min at 4 °C to remove cellular debris. The lysate was filtered through a 0.45 μm filter and ultracentrifuged at 45,000 rpm for 50 min through a 35% (w/v) sucrose cushion. The resulting pellet was resuspended in lysis buffer and purified by size exclusion chromatography on an S-500 Sephadex column using a BioRad Biologic Duoflow FPLC. Fractions were analyzed for purity by sodium dodecyl sulfate−polyacrylamide gel electrophoresis (SDS−PAGE) and concentrated by ultracentrifugation and resuspended by rocking into a chosen buffer.

Size Exclusion Chromatography−Multiangle Light Scattering. Samples were separated on a Wyatt Technologies WTC-200S 5 μM, 2000 Å, 7.8 × 300 mm size exclusion column using an Agilent 1200 HPLC with a flow rate of 0.7 mL/min in a 50 mM sodium phosphate, 100 mM sodium chloride, 200 ppm sodium azide, and pH 7.2 buffer. Samples were detected using an Agilent UV−vis detector, a Wyatt HELEOS multiangle light scattering (MALS) detector, and an Optilab rEX differential refractometer. The number average molecular weight (M_n) of VLPs was calculated using Astra 5.3.14 software (Wyatt Technology Corporation) based on the molecular weight distribution. Equation 1 was used to calculate the molecular weight

$$M = \frac{R(\theta)}{\frac{4\pi^2 n_0^2}{N_A \lambda_0^4}\left(\frac{dn}{dc}\right)^2 cP(\theta)} \quad (1)$$

$R(\theta)$−the excess Rayleigh ratio from the solute, n_0−the solvent refractive index, N_A−Avogadro's number, λ_0−the vacuum wavelength of incident light, (dn/dc)−the specific refractive index increment in mL/g (for proteins: 0.1850), M−the molar mass in g/mol, c−the solute concentration (w/v), and $P(\theta)$−the form factor relating to angular variation and mean square radius.

Denaturing SDS−PAGE. Samples for SDS−PAGE were prepared by adding 20 μL of the sample to 10 μL of the SDS loading dye. Samples were heated at 100 °C for 12 min before loading onto a 12% acrylamide gel. Gels were run at a constant current of 36 A for 50 min. Gels were stained with Coomassie blue, destained, and imaged using a UVP MultDoc-IT digital imaging system.

Transmission Electron Microscopy. Formvar-coated grids (Electron Microscopy Sciences) were glow discharged and exposed to 7 μL protein solution for 1 min. Grids were then washed through exposure to 7 μL water for 1 min, followed by staining with 2% uranyl acetate for 1 min. Excess liquid was wicked away with a filter paper after each step. Images were taken using a JEOL 1010 transmission electron microscope at an accelerating voltage of 80 kV.

Preparation of Poly(allylamine)-Coated VLPs (P22@PAH). 1 mL of P22 VLPs (10 mg/mL in water) was added to poly(allylamine)

https://doi.org/10.1021/acs.biomac.1c00208
Biomacromolecules XXXX, XXX, XXX−XXX

HCl (Millipore-Sigma) in water to a final concentration of 1 mg/mL P22 VLP and 500 PAH chains per VLP (13.8 μM). The P22@PAH solution was rocked at room temperature for 2 h and then dialyzed overnight against water across a 50 kDa molecular weight cutoff (MWCO) membrane.

Preparation of G6 PAMAM Dendrimer-Coated VLPs (P22@G6). 1 mL of P22 VLPs (10 mg/mL in water) was added to the G6 PAMAM dendrimer (Millipore-Sigma) in water to a final concentration of 1 mg/mL P22 VLP and 400 G6 dendrimers per VLP (11.1 μM). The P22@G6 solution was rocked at room temperature for 2 h and then dialyzed overnight against water across a 50 kDa MWCO membrane.

Ionic Strength Aggregation Screen. 10 μL of P22 VLPs (10 mg/mL in water) was added to 90 μL of G6 (11.08 μM final concentration) or PAH (13.84 μM final concentration) in NaCl solution. The NaCl concentration depicted is the final concentration of NaCl in the experiment. Polymer concentrations were the same as used for P22@polymer preparation. Samples were left to stand at room temperature overnight, then analyzed on an Agilent Cary 8454 UV−vis Spectrophotometer.

Polymer/P22 Ratio Cluster Analysis. 15 μL of P22 VLPs (10 mg/mL in water) was added to 135 μL of G6 or PAH in water. The polymer concentration was varied based on the ratio of polymer to P22 VLPs (between 346 nM and 138.5 μm final polymer concentration). The samples were incubated at room temperature overnight and analyzed by dynamic light scattering (DLS).

DLS and Zeta Potential Measurements. DLS and Zeta potential measurements were carried out on a Malvern Instruments Zetasizer Nano ZS. The protein concentration was approximately 0.1 mg/mL. For zeta potential measurements, all samples were in water. The Smoluchowski approximation was used to convert the electrophoretic mobility to zeta potential.

Sample Preparation for Small-Angle X-ray Scattering Measurements. Samples of P22, P22@PAH, and P22@G6 were dialyzed against water and adjusted to a total VLP concentration of 0.8 mg/mL. Background subtraction was carried out by subtracting the scattering data from water from the last dialysis of each sample from the sample data.

SAXS Measurements. Small-angle X-ray scattering (SAXS) measurements were performed at beamline 12 ID-B at the Advanced Photon Source, Argonne National Lab. Measurements were conducted at 14 keV and the scattering data were collected using a Pilatus 2 M detector. The scattering angle was calibrated using silver behenate as a standard. One-dimensional scattering profiles were obtained by averaging two-dimensional scattering patterns. The data were represented as scattering intensity as a function of scattering vector q

$$q = \frac{4\pi}{\lambda} \sin\theta$$

where θ is half of the scattering angle 2θ and λ is the X-ray wavelength used for measurements.

Pair distance distribution functions $p(r)$ were determined using PRIMUS.[36]

Determination of Concentrations by UV−vis Spectroscopy. Sample concentrations were determined through absorbance measurements on an Agilent Cary 8454 UV−vis Diode Array System. Protein concentrations were measured using extinction coefficients at 280 nm calculated using the Expasy ProtParam tool after 1:10 dilution in 6 M guanidine HCl to denature proteins. For PAH- or G6-coated particles, samples were first diluted with 4 M NaCl to remove contribution to absorbance readings from scattering. Concentrations of NADH and NADH-dendrimer conjugates were measured using ε_{340} = 6.22 mM^{-1} cm^{-1}.

Calculation of P22 CP Subunit Electrostatic Map. The electrostatic map was calculated from the P22 procapsid model (PDB: 2XYY) using the Adaptive Poisson—Boltzmann Solver (APBS).[37] The solvent conditions for the calculation were 100 mM NaCl in water, and the dielectric constant of the solvent was 78.54.

Synthesis of NADH-Den Conjugates. *8-NAD$^+$−Br.* The first step of the reaction was the bromination of NAD$^+$ at the C8 position of adenine. NAD$^+$ (5.00 g, 7.55 mmol) was dissolved in pH 4.5 50 mM sodium acetate buffer (60 mL) at room temperature. Reaction was stirred under argon as bromine (2.0 mL, 39.05 mmol) was added dropwise to solution. Reaction was allowed to proceed overnight. Note: The reaction still worked when completed without argon. We have found that a precipitate formed upon the addition of bromine that contributed to a lower yield of our product. The completion of the reaction was monitored by changes in the UV absorbance, where λ_{max} shifted from 259 to 265 nm (Figure S4) and further verified using H^1 NMR through the disappearance of the C8 proton peak (Figure S6).[38] For this step, it was important to protect NAD from electrophilic attack at the C5 position of the nicotinamide; therefore, the oxidized form (NAD$^+$) was used. The mixture was washed with carbon tetrachloride until the organic layer showed little to no color. The aqueous phase was recovered and dialyzed into water overnight using a 500 MWCO cellulose dialysis tubing (Spectrum Labs). The resulting solution was lyophilized for 48 h and the product was recovered as a light-yellow powder (3.09 g, 52% yield).

^{1}H NMR (400 MHz, D_2O): δ 9.25 (s, 1H), 9.10 (d, 1H), 8.75 (d, 1H), 8.20 (t, 1H), 8.1 (s, 1H), 6.10 (d, 1H), 5.95 (d, 1H), 4.0−4.5 (m, 9H). The full NMR spectrum is available in Figure S5.

8-NADH−Br. At this point in the synthesis, NAD$^+$ was reduced to NADH, which is more thermally stable as the C2 and C6 of nicotinamide of NAD$^+$ are especially prone to nucleophilic attack, which was important to avoid in the following step. 8-NAD$^+$−Br (351.3 mg, 0.487 mmol) was dissolved in 18 mL of 1.3% (v/w) sodium bicarbonate buffer using a 2-neck RBF. Solution was stirred while bubbling the argon gas through solution for 30 min. Using other neck of RBF, sodium dithionite (175.6 mg) was added while continuing to bubble argon. The resulting mixture was stirred under argon gas for 3 h at room temperature, monitored by the appearance of a peak at 340 nm in the UV spectrum (Figure S4) and verified using H^1 NMR through the upfield shift of the nicotinamide protons (Figure S8). The remaining sodium dithionite was oxidized by removing the flow of argon and stirring while exposed to air for 1 h. The completion of reaction was monitored by measuring the A_{265} to A_{340} ratio and the reaction stopped when the ratio approached ∼3. The product was recovered by precipitating with 10× cold acetone (stored in −20 °C) and centrifuging at 4500 × g for 5 min. The supernatant was decanted through a filter. The remaining pellet was dissolved in water and lyophilized for 48 h. The product was recovered as a beige solid (430 mg). ^{1}H NMR (400 MHz, D_2O): δ 8.1 (s, 1H), 6.82 (s, 1H), 6.18 (d, 1H), 5.80 (d, 1H), 4.0−5.0 (m, 11H), 2.9 (m, 2H). The full NMR spectrum is available in Figure S7.

8-NADH−NH$_2$. 8-NADH−Br (321 mg, 0.408 mmol) was added to 6 mL DMSO and heated to 60 °C. In a different flask, 2,2'-(ethylenedioxy)*bis*(ethylamine) = linker (1.285 g, 8.32 mmol) was dissolved in 6 mL of DMSO and also heated to 60 °C. The solution containing 8-NADH−Br was added to the solution containing a linker. The resulting mixture was stirred under a condenser at 80 °C for 6 h. The reaction was cooled to room temperature, and the acetone precipitation was repeated by adding 120 mL of cold acetone and the precipitate was recovered using centrifugation (4500 × g, 5 min). The pellet was dissolved in water and lyophilized to dry. Powder was recovered as a beige solid (318 mg, 60% yield). Yield was calculated based on A_{340}. ^{1}H NMR (400 MHz, D_2O): δ 8.2 (s, 1H), 6.75 (s, 1H), 5.85−6.10 (m, 2H), 5.25 (dd, 1H), 3.8−4.5 (m, 9H), 3.1−3.5 (m, 13H), 2.80 (d, 2H) 1.01 (t, 1H). The NMR spectrum is available in Figure S9. Calculated high-resolution mass spectrometry for $C_{27}H_{42}O_{16}N_9P_2$ 810.2225, observed 810.2223. Calculated HRMS for $C_{27}H_{41}O_{16}N_9NaP_2$ 832.2044, observed 810.2043. The MS result is available in Figure S11.

NADH−Den$^-$. All syntheses for the conjugation proceeded using the same reaction scheme with varying stoichiometric amounts of dendrimer. The theoretical number of NADH molecules per dendrimer was a 2:1 molar ratio. The concentrations of NADH were determined using A_{340}. The 8-NADH−NH_2 amount was adjusted to 50 mg (61.6 μmols) and kept constant for all reactions.

https://doi.org/10.1021/acs.biomac.1c00208
Biomacromolecules XXXX, XXX, XXX−XXX

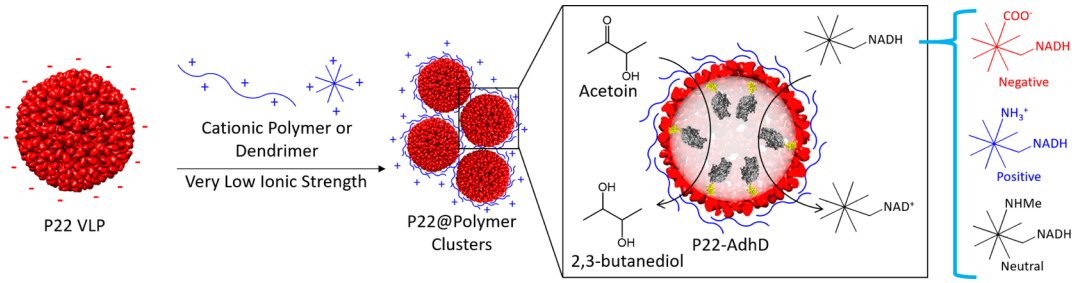

Figure 1. Scheme of P22 procapsid VLP (PDB: 2XYY) interaction with cationic macromolecules and probing of the effect of low ionic strength conditions on the ability of VLPs to uptake charged substrates.

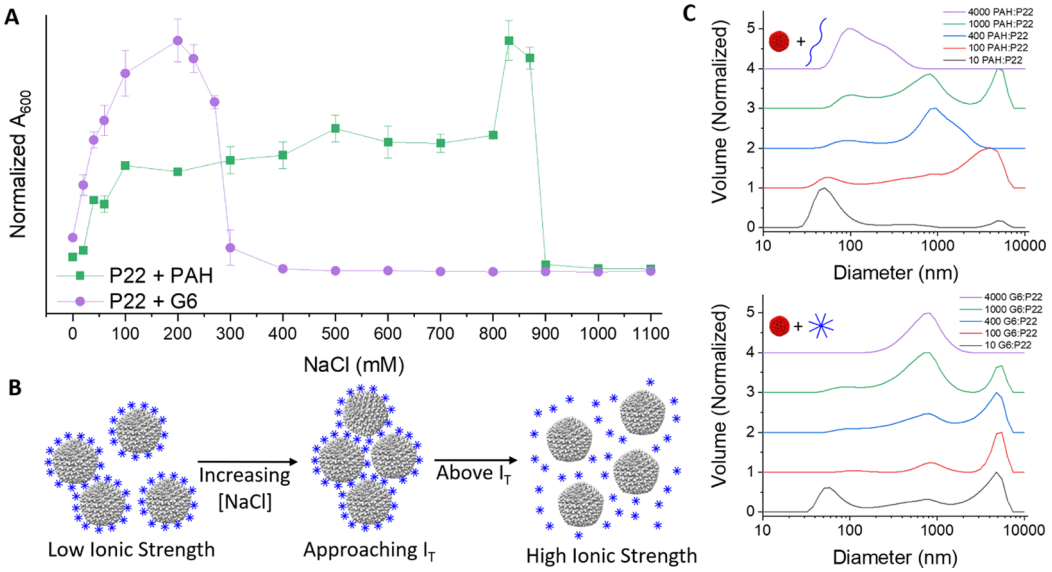

Figure 2. (A) Assembly of P22 with PAH or G6 monitored by measuring the absorbance at 600 nm (A600) at different ionic strengths. Note the low scattering at low ionic strength and the sharp drop in scattering at the threshold ionic strength (270 mM for P22 + G6 and 870 mM for P22 + PAH). (B) Scheme of P22 interaction with the cationic dendrimer for a range of ionic strengths. (C) DLS data for different ratios of P22 VLPs and PAH (top) or G6 (bottom).

As a representative example: The Gen. 2.5 dendrimer (7.7 μmols) was dissolved in 3 mL of pH 4.7 100 mM MES Buffer, EDC (0.0145 g, 75 μmols) was added to the reaction and stirred for 1 h, and 8-NADH–NH_2 was dissolved in the MES buffer (3 mL) and added to the solution containing dendrimers. The mixture was stirred overnight and purified using a cellulose dialysis tubing with a MWCO of 3.5 kDa. The product was lyophilized and stored at 4 °C until use. The NMR spectrum is available in Figure S12.

NADH–Den^0. All syntheses for the conjugation proceeded using the same reaction scheme with varying stoichiometric amounts of methylamine and EDC. The molar ratios for EDC and methylamine were in 10-fold excess of theoretical values of dendrimer terminal carboxylic acid groups. As a representative example: NADH–Den$^-$ (3.85 μmols) was dissolved in pH 4.7 100 mM MES Buffer with EDC (0.234 g, 1.232 mmols) and stirred for 1 h at room temperature. Methylamine (0.038 g, 1.232 mmols) was added to the reaction and stirred overnight and purified using the same type of dialysis tubing as was used in the synthesis of NADH–Den$^-$.

NADH–Den$^+$. The molar ratios for EDC and ethylenediamine were in 10-fold excess of theoretical values of dendrimer terminal carboxylic acid groups. NADH–Den$^-$ (3.85 μmols) was dissolved in 3 mL of pH 4.7 100 mM MES Buffer with EDC (0.234 g, 1.232 mmols) and stirred for 1 h at room temperature. Ethylenediamine (0.074 g, 1.243 mmols) was dissolved in 2 mL of the same buffer and the solution containing NADH–Den$^-$ was added. The solution was stirred overnight and purified using 3.5 kDa MWCO dialysis.

Kinetics of NADH Oxidation by AdhD. Enzyme kinetics data were collected on a BioTek Cytation 5 Cell Imaging Multi-Mode Reader. The acetoin concentration was varied from 1 to 200 mM. The concentration of NADH or NADH–Den was 220 μM. To initiate the reaction, protein was added to a final enzyme concentration of 650 nM. The samples were shaken using the orbital shaking function on the plate reader for 30 s, followed by monitoring of the absorbance at 340 nm (NADH oxidation) and 600 nm (aggregate formation). Path length correction was used to correct for the sample depth on the 96-well plates. At least three replicates were collected for each data point.

Kinetics data were analyzed using OriginPro. Initial reaction velocities were found using the Tangent function, followed by fitting of the acquired data to a standard Michaelis–Menten model (eq 2) to determine k_{cat} and K_M.

$$y = \frac{v_{max}[C]}{K_M + [C]} \quad (2)$$

v_{max}–Maximum velocity, [C]–substrate (acetoin) concentration, and K_M–Michaelis constant (concentration at 1/2 v_{max}).

Bead Adsorption. 2.0 μm carboxylate-modified polystyrene beads (100 μL, stock concentration 25 mg/mL) were centrifuged at 10,000 × g for 10 min and redissolved in 20 mM tris, pH 7.2 to a final concentration of 5 mg/mL. P22, P22@PAH, or P22@G6 (final concentration 0.5 mg/mL) were added to the polystyrene beads (final concentration 0.5 mg/mL) and incubated for 30 min. The solution was centrifuged for 5 min at 10,000 ×g. The pellet consisting of beads and bound protein was resuspended in the original volume of 20 mM tris buffer. 15 μL aliquots of the pellet solution, the supernatant, and a 0.5 mg/mL control consisting of P22, P22@PAH, or P22@G6 with

https://doi.org/10.1021/acs.biomac.1c00208
Biomacromolecules XXXX, XXX, XXX–XXX

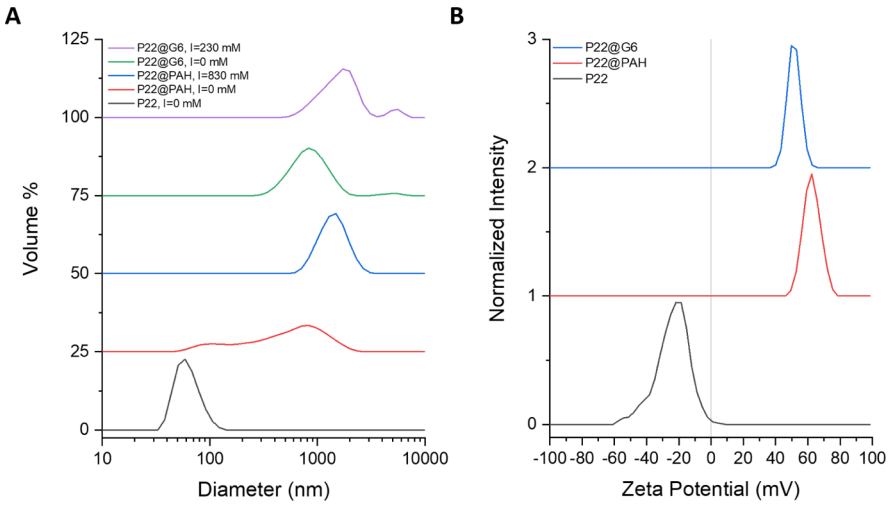

Figure 3. (A) DLS analysis of P22@polymer clusters and their components. The addition of the polymer species to P22 causes the formation of aggregates composed of multiple VLPs as a result of kinetic traps during mixing. (B) Zeta potential analysis of P22@polymer clusters and their components. The high positive surface charge of the clusters indicates that the polymeric species coat the VLPs.

no beads were added to 5 μL of the SDS−PAGE loading dye, boiled for 10 min, and centrifuged after cooling to avoid concentration of the sample by evaporation. 15 μL of each of the samples was then run on an SDS−PAGE gel.

RESULTS AND DISCUSSION

Ionic Strength Dependence of P22−Polymer Interactions. As a model system to investigate the interactions between charged macromolecules and protein materials at low ionic strength, we studied the interaction between P22 VLP nanoreactors and cationic polymers. We used two different polymers to investigate the effect of polymer morphology—the nominally spherical G6 polyamidoamine (PAMAM) dendrimer and linear 15 kDa polyallylamine HCl (PAH). In addition, the porous P22 nanoreactors contained an encapsulated catalytically active enzyme, which allowed us to investigate the effect of both the capsid and the polymer coating on access by large macromolecular substrates to the sequestered enzyme at low ionic strength (Figure 1).

Negatively charged VLPs experience Coulombic attraction to positively charged polymers, allowing for mediation of the attractive forces through ionic strength.[30,39] To investigate the effect of ionic strength on these interactions, P22 VLPs were added to solutions of G6 PAMAM dendrimers (G6) or 15 kDa polyallylamine chains (PAH) at varying ionic strengths (Figure 2A). As a proxy for light scattering, the optical density at 600 nm was monitored to determine the degree of formation of the P22-polymer assembly. Particles assemble below the threshold ionic strength I_T, above which the attractive electrostatic interactions are screened by ions in solution.[31,33] The degree of light scattering is highest just below I_T, indicating that the formation of the largest assemblies occurs when the attractive forces between particles are weak. At low ionic strength, the scattering is low, suggesting that the P22-polymer assemblies are small.

Previously published simulations of P22 interactions with G6 predict that at a very low ionic strength (I < 30 mM), the positively charged dendrimers will conformally coat the negatively charged VLP, resulting in individual VLP particles with tightly bound dendrimers contributing to overall charge reversal.[35] The strong attractive forces between P22 and G6 limit the dissociation and re-entry into bulk solution of the dendrimer once it associates with P22, leading to a slow exchange rate between the VLP-bound and unbound polymer and preventing the exposure of negative patches, which would act as bridging sites.[35] In the simulation, this leads to the stable coating of individual VLPs with the dendrimer in a core@shell structure, and the formation of clusters of multiple VLPs is prevented by the strong association between the VLP and the polymer and the slow exchange between free and bound polymers.

To experimentally investigate the interaction between PAH or G6 and P22 at low ionic strength, we incubated P22 VLPs with different amounts of polymer and studied the product by DLS. The polymer:P22 ratio was varied to determine the effect of the polymer concentration on the size of the P22-polymer hybrid material (Figure 2C). At a very low polymer:P22 ratio of 10 polymers per VLP, peaks were seen at both 60 nm and at large sizes, indicating that while many VLPs are remained free as individual particles, clusters of VLPs held together by polymers were present. Previous work at high ionic strength has shown that a minimum of 24 G6 adsorbed to P22 is necessary for assembly into larger structures, explaining the presence of the unincorporated particles.[35] The 60 nm peak was no longer seen at higher polymer/P22 ratios, indicating the incorporation of all the VLPs into the clustered material. The structures formed at very high polymer/P22 ratios were smaller than at intermediate ratios, but still significantly larger than individual VLPs. This suggests that at even higher polymer/P22 ratios, single polymer-coated VLPs may be accessible.[40]

Previous simulation of the P22-G6 interaction investigated polymer/P22 ratios between 25 and 1000 and suggested that at low ionic strength, cationic polymers would coat P22 VLPs to yield single-coated particles. At similar stoichiometries tested here, we found that the addition of P22 to a polymer solution produced clusters of particles, in contrast to the single particles expected from the simulation. Experimentally, the kinetics of mixing VLPs with polymer solution leads to instances where partially coated VLPs encounter uncoated, or partially coated, VLPs and result in some bridging interactions and the observed clustering (Figure 2B). At higher ionic strengths, the clusters are large, indicating the presence of

https://doi.org/10.1021/acs.biomac.1c00208
Biomacromolecules XXXX, XXX, XXX−XXX

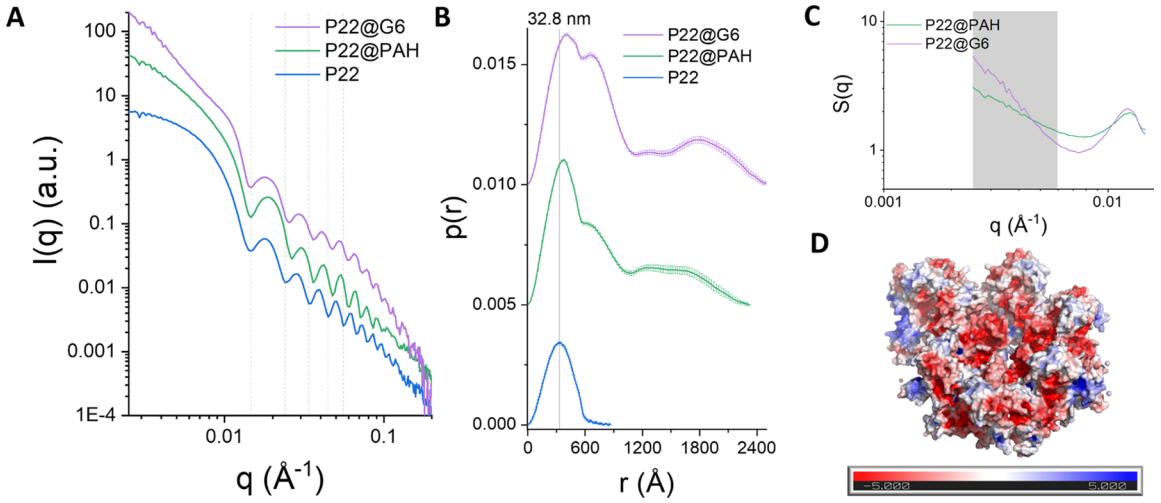

Figure 4. SAXS analysis of P22 VLPs and P22@polymer clusters. (A) Background-subtracted SAXS scattering profiles for P22, P22@PAH, and P22@G6. Scattering profiles are offset to allow for easier viewing. (B) Extracted pair distance distribution functions for P22 and P22@polymer clusters showing the radius of species in solution. The first peak on each $p(r)$ corresponds to single VLPs (coated with the polymer, if applicable), while larger peaks indicate the presence of clusters of VLPs held together by interactions with cationic polymers. (C) Structure factor for the P22@polymer samples. The linear region used for Porod analysis is shaded in gray. (D) Electrostatic map of the P22 asymmetric unit.[42] Negatively charged regions, which may associate electrostatically with PAH or G6, are colored in red. Units on the color bar are in k_BT/e, where k_B is the Boltzmann constant, T is the temperature in Kelvin, and e is the elementary charge.

bridging interactions arising from the exchange of polymers between the bulk solution and the P22 surface to form a thermodynamically favored product. The formation of the small clusters present at low ionic strength is likely the result of a kinetic process in which polymers are trapped on the charged capsid surface. The difference in product formation at low versus high ionic strength indicates that the effect of charge screening on the interactions of charged molecules with P22 VLPs is different at low ionic strength.

At ionic strengths just below I_T, P22 and G6 assemble into large structures, but the same stoichiometry at low ionic strength yields smaller clusters. While experimental studies have investigated the structure and catalytic behavior of large aggregate materials assembled at this stoichiometry at high ionic strength, the behavior of the clusters formed at low ionic strength has been unexplored. Investigation of the catalytic activity of P22 arrays assembled with G6 at high ionic strength showed no difference in activity between VLPs free in solution or condensed within the G6-induced array.[31] However, the effect of electrostatic interactions on this catalytic activity is screened by the high solution ionic strength.

We chose to explore the clusters formed at a G6/P22 ratio of 400 to better understand the size, surface charge, structure, and catalytic behavior of protein-based materials at low ionic strength. For P22-polymer materials prepared with PAH, we used a PAH/P22 ratio of 500, which kept the total number of ionizable groups on the surface of the polymer species in solution the same as for samples previously prepared with G6. P22 particles in water were added to G6 or PAH in water and allowed to equilibrate during dialysis overnight. The resulting material (P22@G6 or P22@PAH, respectively) was analyzed by DLS and zeta potential measurements, as well as SAXS to elucidate the structure of the clusters.

Structural Analysis of P22@polymer Clusters. DLS measurements show that P22@G6 and P22@PAH are significantly larger than individual uncoated VLPs, indicating that the polymers initiate the formation of clusters of VLPs (Figure 3). DLS of P22@PAH suggests the presence of two populations of particles—a minor peak corresponding to small clusters (~105 nm) and a larger major peak (~820 nm). For P22@G6, one major peak dominates (~820 nm), with a smaller peak at a higher particle size (~4800 nm). For both polymer types, the products formed just below the threshold ionic strength are larger than those formed at low ionic strength. This suggests that at low ionic strength, the reorganization of VLP clusters into larger structures is prevented by the strong electrostatic interactions, which keep the polymer coating adsorbed to P22. Zeta potential measurements of the P22@polymer in water show a surface charge reversal from the negative, uncoated P22 VLPs to high positive charge on P22@polymer clusters. The charge inversion on P22@polymer clusters demonstrates that the outer layer of the structures is comprised of the cationic polymer, consistent with our core−shell model.

We used SAXS to show the formation of a layer of cationic polymers on P22 and interrogate the structure of the P22@G6 and P22@PAH clusters (Figure 4A). The structure factor component of the scattering profile is weak, indicating that the clusters do not have a long range order and are most likely the kinetic product of aggregation. Analysis of the pair distance distribution function $p(r)$ revealed several peaks corresponding to the hydrodynamic radius (R_H) of P22@polymer clusters (Figure 4B). The first peak of $p(r)$ for the P22@polymer samples shows a slight increase in the particle radius from 32.8 nm for uncoated P22 to 38.0 nm for P22@PAH and 41.0 nm for P22@G6. This initial peak likely corresponds to single P22 VLPs coated with G6 or PAH. Larger peaks (around 60, 130, and 160 nm) correspond to clusters of multiple VLPs held together through electrostatic interaction with polymers. The polydispersity of the P22@polymer clusters is likely a result of kinetic trapping during the addition of P22 to the polymer solution, where clusters larger than a single polymer-coated VLP likely form before the VLPs are fully coated. Due to the low exchange rate between the polymer adsorbed to P22 and the polymer in bulk solution, it is unlikely that the clusters are

https://doi.org/10.1021/acs.biomac.1c00208
Biomacromolecules XXXX, XXX, XXX−XXX

the result of an annealing or ripening process such as those seen close to I_T.

The increase in the particle radius from bare P22 to polymer-coated VLPs is shown in the first $p(r)$ peak to be 8.2 nm for P22@G6 and 5.2 nm for P22@PAH. The 8.2 nm increase in the particle radius between uncoated P22 and P22@G6 is close to the R_H for individual G6 dendrimers (6.7 nm). This corresponds to simulation models in which G6 adsorbs to P22 VLPs in a monolayer of spheres. Because the dendrimer is roughly spherical, it may not fit into the grooves and ridges of the P22 coat protein (Figure 4D). Most of the negative charge of the capsid exterior is localized in these regions, while the tops of the ridges pointing away from the capsid are more neutral. Because PAH is a linear polymer, it is both more flexible and thinner than G6, possibly allowing it to intercalate between the ridges of the coat protein into regions of high negative charge. This also means that the polymer may not wrap around the capsid as might be possible for a perfectly spherical capsid, but instead could be partially adsorbed to the capsid with small areas free in solution. This explains why the increase in size between bare P22 and P22@PAH is smaller than the effective polymer length of 18 nm, but larger than the simple PAH chain diameter of 1.2 nm.[41] The loose polymer ends are free in solution, allowing for bridging between capsids to form clusters of P22 during mixing.

This localization would lead to a smaller distance between anionic amino acid residues and charged amines on PAH than the surface amines on G6. As electrostatic forces are dictated by Coulomb's law, this difference in distance could lead to stronger attraction between P22 and PAH than between P22 and G6. This is reflected by the I_T values for each, where the interaction between P22 and G6 is interrupted at 270 mM NaCl, but the interaction of P22 with PAH persists until 870 mM NaCl.

Analysis of the structure factor $S(q)$ provides more information on the structure of the VLP@polymer clusters. The 1st order peak of $S(q)$ corresponds to the nearest neighbor distance between VLPs in clusters. This spacing is 50.2 nm for P22@PAH and 51.7 nm for P22@G6. The size of the clusters can be roughly estimated by the Scherrer equation for the 1st order peak and is about 200 nm both for P22@PAH and P22@G6, indicating that there are about 64 VLPs per a cluster. However, comparison of the lowest q intensity of $S(q)$, which is proportional to the number of VLPs in a cluster, indicates that P22@G6 has at least twice many VLPs in a cluster. Porod analysis of the linear region of the structure factor indicates slopes of 0.91 for P22@PAH and 1.79 for P22@G6. These slopes correspond to an aggregate shape of a rod for P22@PAH clusters and a polymer coil for P22@G6 (Figure S16). Because the size of P22@PAH is similar to that of P22@G6 despite the larger number of VLPs per cluster in P22@G6, the shape of the structures explains the more open packing of VLPs in P22@PAH. The smaller number of particles per cluster and more open VLP packing for P22@PAH likely arise from stronger interaction between PAH and P22 than between G6 and P22, which is also supported by the higher I_T for PAH than G6. When the interaction is stronger, the clusters assemble more quickly into smaller products with a more open structure and cannot rearrange into larger, more densely packed structures.[34]

Charge-Dependent Adsorption of P22 and P22@polymer Clusters. P22 VLPs have been shown here and elsewhere to be a suitable component for higher-order material assembly. These materials often use the negatively charged exterior of the capsid as a key part of the self-assembly strategy. To show that the charge reversal by PAH or G6 on P22 changes the ability of the nanoreactors to adsorb to charged surfaces, we incubated each material with negatively charged carboxylate-modified polystyrene beads (Figure S17). The beads were separated by centrifugation and the bound material and supernatant were analyzed by SDS−PAGE (Figure 5, Table S1). P22-AdhD did not bind strongly to the beads due to repulsive interactions between the capsid and the negatively charged beads and the majority of the material was present in the supernatant. P22@PAH and P22@G6 were found in both the pellet and the supernatant, indicating binding between the cation-coated VLPs and the beads. The difference between adsorption to the bead between the G6-coated and PAH-coated VLPs likely arises from the availability of the sterically bulky G6 dendrimer for interaction with the bead. Because G6 is large and spherical, it protrudes more from the VLP surface, while PAH is more tightly adsorbed and less accessible for interaction with the bead. This result shows that the polymer coating changes the adsorption of P22 VLPs, demonstrating their use as a building block in materials where uncoated P22 VLPs may be unsuitable due to their negative charge.

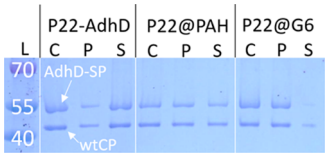

Figure 5. SDS−PAGE gel showing adsorption of P22@polymer onto negatively charged beads. From left to right, lanes show a protein control with no exposure to beads (C), the pellet after exposure to the indicated VLP material (P), and the supernatant after centrifugation of the beads (S).

Determination of the Effect of Polymer Coatings on P22 Nanoreactors at Low Ionic Strength. As a model for the behavior of enzyme-based materials in a nonphysiological environment and to determine the effect of the polymer on the VLP as a charge-inverse building block, we studied and compared the activity of the enzyme alcohol dehydrogenase D (AdhD) encapsulated within P22 in the P22@polymer clusters, encapsulated within P22 VLPs, and free in solution. We monitored the activity of AdhD toward the reduction of acetoin and oxidation of nicotinamide adenine dinucleotide (NADH). Here, enzyme kinetics were examined in water (pH 6.4) and in low ionic strength buffer (20 mM tris, pH 7.2, κ^{-1} = 2.28 nm) to control for pH variations when using water as a solvent. To compare kinetic constants between the hierarchical VLP materials more easily, we calculated the ratio between the higher-order material and its building block (e.g., P22@polymer/encapsulated enzyme or encapsulated/free enzyme). All kinetic constants are provided in Table 1.

Catalytic Activity of AdhD toward NADH is Maintained at Low Ionic Strength for the Enzyme within P22@polymer Clusters, Encapsulated Enzyme, and Free Enzyme. Low ionic strength oxidation of NADH by AdhD showed very similar activity for all levels of hierarchical organization of the enzyme including P22@polymer, P22, and AdhD-free (Figure 6).

The k_{cat} ratios for both VLP@polymer types show small changes between the polymer-coated VLPs and the uncoated

https://doi.org/10.1021/acs.biomac.1c00208
Biomacromolecules XXXX, XXX, XXX−XXX

Table 1. Kinetic Parameters for the Oxidation of Unmodified NADH, NADH−Den$^-$, NADH−Den$^+$, and NADH−Den^0 by P22@polymer Clusters and Their Components[a]

substrate	solution	material	k_{cat} (s^{-1})	K_M (mM)
unmodified NADH	water	P22@PAH	0.108 ± 0.0067	28.68 ± 3.77
		P22@G6	0.094 ± 0.0112	19.69 ± 5.35
		P22−AdhD	0.094 ± 0.011	29.76 ± 0.007
		AdhD−SP	0.077 ± 0.007	28.24 ± 5.27
	20 mM Tris	P22@PAH	0.042 ± 0.0069	7.99 ± 3.35
		P22@G6	0.032 ± 0.0047	7.59 ± 3.93
		P22−AdhD	0.058 ± 0.004	3.56 ± 0.204
		AdhD−SP	0.042 ± 0.001	1.52 ± 0.102
NADH−Den^0	water	P22@PAH	0.14655 ± 0.044	127.35 ± 63.5
		P22@G6	0.127 ± 0.01278	70.57 ± 17.05
		P22−AdhD	0.0674 ± 0.0224	114.5 ± 70.9
		AdhD−SP	0.045 ± 0.0094	43.4 ± 18.4
	20 mM Tris	P22@PAH	0.0735 ± 0.016	11.35 ± 12.1
		P22@G6	0.0339 ± 0.0013	0.732 ± 0.56
		P22−AdhD	0.024 ± 0.005	16.45 ± 11.41
		AdhD−SP	0.0102 ± 0.0006	1.29 ± 0.41
NADH−Den$^-$	water	P22@PAH	0.107 ± 0.087	222.2 ± 227.1
		P22@G6	*	*
		P22−AdhD	0.076 ± 0.028	233.8 ± 138.9
		AdhD−SP	0.016 ± 0.0018	2.58 ± 1.57
	20 mM Tris	P22@PAH	0.0177 ± 0.0019	17.18 ± 5.16
		P22@G6	0.0418 ± 0.0146	64.81 ± 48.2
		P22−AdhD	0.02 ± 0.0025	4.28 ± 2.8
		AdhD−SP	0.011 ± 0.00036	0.96 ± 0.16
NADH−Den$^+$	water	P22@PAH	**	**
		P22@G6	**	**
		P22−AdhD	**	**
		AdhD−SP	**	**
	20 mM Tris	P22@PAH	0.0281 ± 0.0289	113.7 ± 156.2
		P22@G6	*	*
		P22−AdhD	0.014 ± 0.00099	11.17 ± 2.47
		AdhD−SP	0.0088 ± 0.001	3.13 ± 1.6
unmodified NADH[28]	100 mM NaP, pH 6.1, 50 °C	P22−AdhD	0.770 ± 0.031	6.23 ± 0.87
		AdhD−SP	0.097 ± 0.005	1.23 ± 0.31

[a]Parameters for which kinetic constants could not be determined due to aggregation are marked with an asterisk (*). Parameters for which enzymatic activity was not detected are marked with double asterisks (**). The original Michaelis−Menten curves are available in Figures S18 and S19.

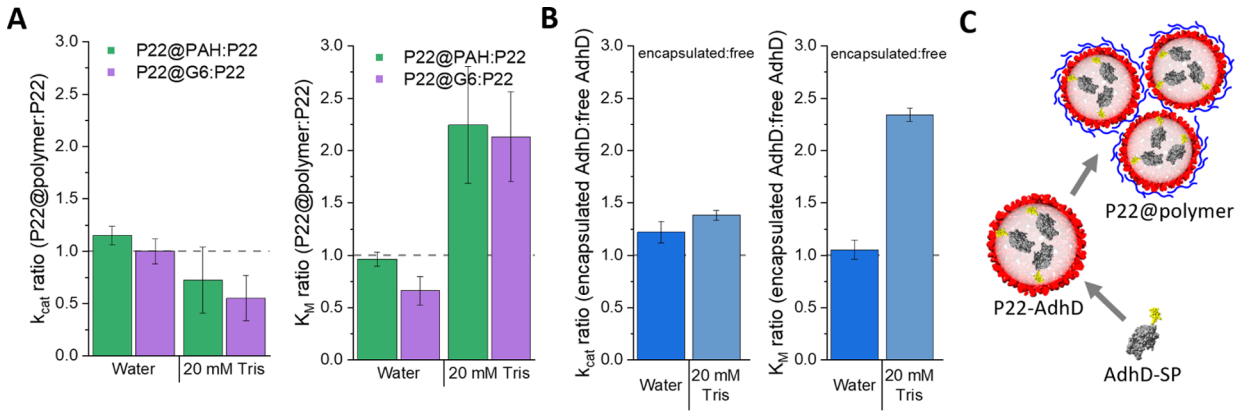

Figure 6. Michaelis−Menten kinetic constant ratios for NADH oxidation by hierarchically ordered P22@polymer materials. (A) k_{cat} and K_M ratios for P22@polymer/P22 kinetic constants. (B) k_{cat} and K_M ratios for encapsulated AdhD−SP/free AdhD−SP kinetic constants. (C) Scheme showing the levels of hierarchical organization in these enzyme-based material assemblies.

VLPs (Figure 6A). The K_M ratios show no change in water and a slight increase in 20 mM tris. Coating with polymers shows that the polymer does not have a significant effect on the enzyme activity or substrate access to the enzyme. The slight change in 20 mM tris may be the result of partial blockage of the P22 pore by the adsorbed polymer, providing some steric

https://doi.org/10.1021/acs.biomac.1c00208
Biomacromolecules XXXX, XXX, XXX−XXX

or electrostatic effect on the diffusion of the small substrate into the capsid, but this difference is not great enough to suggest that the polymer significantly alters the catalytic activity of the P22 nanoreactor building block. This lack of a significant effect on NADH oxidation by the polymer coating indicates that the pores of the P22 capsid are not blocked and that any electrostatic effects from the charged polymer do not prevent the small molecule substrate from entering the capsid.

To assess the role of the VLP in the encapsulated enzyme activity, we compared the ratios of the kinetic constants for P22−AdhD and free AdhD−SP (Figure 6B). The k_{cat} ratios between P22−AdhD and free AdhD−SP also indicate no effect of encapsulation on enzyme activity. The K_M ratio similarly indicates no significant change in K_M in water and only a slight increase upon encapsulation in 20 mM tris. These data suggest that the small NADH molecule can easily access the enzyme through the porous, charged capsid even in low ionic strength solution. Furthermore, the effect of encapsulation on AdhD activity at these ionic strengths toward NADH is negligible.

Together, the k_{cat} and K_M ratios for each level of hierarchical material assembly show that the activity of and substrate access to AdhD by NADH is not affected by either encapsulation within a VLP or polymer coating of the VLP. Furthermore, the small NADH molecule can easily access the enzyme through the porous, charged capsid even in low ionic strength solution. Thus, the charge reversal achieved by polymer association to the exterior of P22 VLPs does not affect the functioning of the nanoreactors, highlighting their potential in functional materials design and construction.

Substrate Charge can be Controlled Through Conjugation of a Dendrimer to NADH. Electrostatic interactions are enhanced under low ionic strength conditions. To investigate the effect of substrate charge on AdhD activity, NADH was conjugated to G2.5 PAMAM dendrimers (NADH−Den). NADH coupled to dendrimers of varying sizes has been used to probe the size dependance of AdhD substrate diffusion through the pore of P22 VLPs.[42] The charge of the NADH−Den conjugate was controlled through modification of the dendrimer surface groups to produce neutral (NADH−Den^0), negatively charged (NADH−Den$^-$), and positively charged (NADH−Den$^+$) conjugates. Each NADH−Den conjugate has approximately 31 surface groups and one NADH molecule. The surface group modification of NADH−Den was monitored by NMR and the surface charge was confirmed by zeta potential measurements (Figures S12−S14). With each variant, the G2.5 dendrimer (approximate R_H = 1.7 nm) was small enough to allow for entry into the capsid.

Substrate Charge Affects Uptake by P22 VLP Nanoreactors. To determine the effect of encapsulation of AdhD within P22 VLPs under low ionic strength conditions, we determined the ratios of kinetic constants for AdhD encapsulated within uncoated VLPs and the free, unencapsulated, AdhD (Figure 7). Under both solution conditions, we found that the k_{cat} and K_M ratios were above 1. The k_{cat} ratios suggest that encapsulation within P22 provides a slight benefit to the catalytic activity of the enzyme, and the K_M ratios indicate that P22 may inhibit substrate access to the enzyme, particularly for negatively charged substrates.

In water, the K_M ratio for oxidation of NADH−Den$^-$ by encapsulated AdhD−SP indicates a significant increase from free enzyme. This increase is smaller, but still present, for the reactions in 20 mM tris. Because the exterior of the pore of the capsid is highly negatively charged, the negatively charged

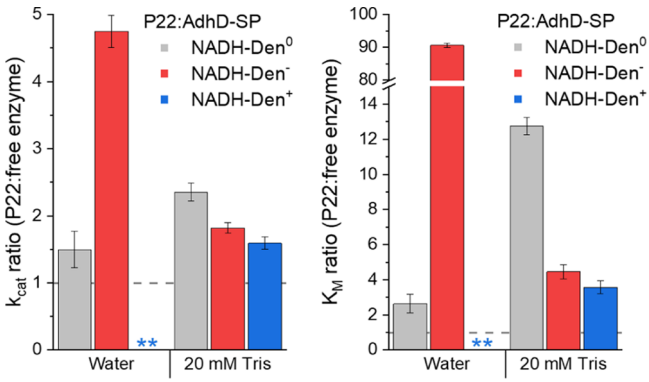

Figure 7. Effect of encapsulation on NADH−Den oxidation. Michaelis−Menten kinetic constant ratios for P22/AdhD−SP. Double asterisks (**) indicate that no enzyme activity was detected.

dendrimer may have difficulty getting through the strong repulsive electric field, causing a low internal concentration of NADH−Den$^-$ and leading to an increase in K_M. Previous studies have shown that a change in the pore structure in VLPs derived from bacteriophage MS2 to incorporate a higher negative charge leads to a similar increase in K_M for a negatively charged substrate.[43] In 20 mm tris, the screening effect from ions in solution likely weakens the interactions between the negatively charged NADH−Den$^-$ and the capsid. Because of this, the ability of the substrate to travel through the capsid pore is less affected by its charge in the buffered solution, leading to a smaller increase in K_M from the free enzyme than in water. The positively charged active site of the encapsulated AdhD−SP may also experience some association with the negatively charged interior-facing surface of the P22 CP. It has been previously established that cargo-SP fusion proteins encapsulated within P22 VLPs localize at the inner capsid surface rather than distributing evenly through the lumen.[44] The increase in K_M seen upon encapsulation for all three NADH−Den variants could, therefore, also be the result of blockage or orientation of the active site away from the substrate due to strong electrostatic attraction to the CP interior surface at low ionic strength.

Neither encapsulated AdhD−SP nor the free enzyme show activity toward NADH−Den$^+$ in water. In 20 mM tris, activity is recovered for both. Like for other NADH−Den, the k_{cat} and K_M ratios are above 1, suggesting that the conditions inside the capsid are slightly more favorable and that the pores of the capsid may somewhat impede access by the substrate due to their high charge.

While the free AdhD is not active toward NADH−Den$^+$ in water, the enzyme showed a strong affinity for NADH−Den$^-$, with a K_M of 2.6 mM compared to a K_M of 43.4 mM for NADH−Den^0. The active site of AdhD contains highly conserved lysine residues, which impart a strong positive charge, facilitating the interaction with the negatively charged phosphate backbone of NADH.[45] As the active site of the enzyme is positive, this drop in K_M is reflective of the strong electrostatic attraction between NADH−Den$^-$ to the active site in water. The drop is not present in 20 mM tris, where the electrostatic interactions between the dendrimer and the active site can be partially screened. Similarly, NADH−Den$^+$ likely experiences electrostatic repulsions from the AdhD active site, preventing enzyme activity in water where the interaction is the strongest. The activity is recovered when the interactions

https://doi.org/10.1021/acs.biomac.1c00208
Biomacromolecules XXXX, XXX, XXX−XXX

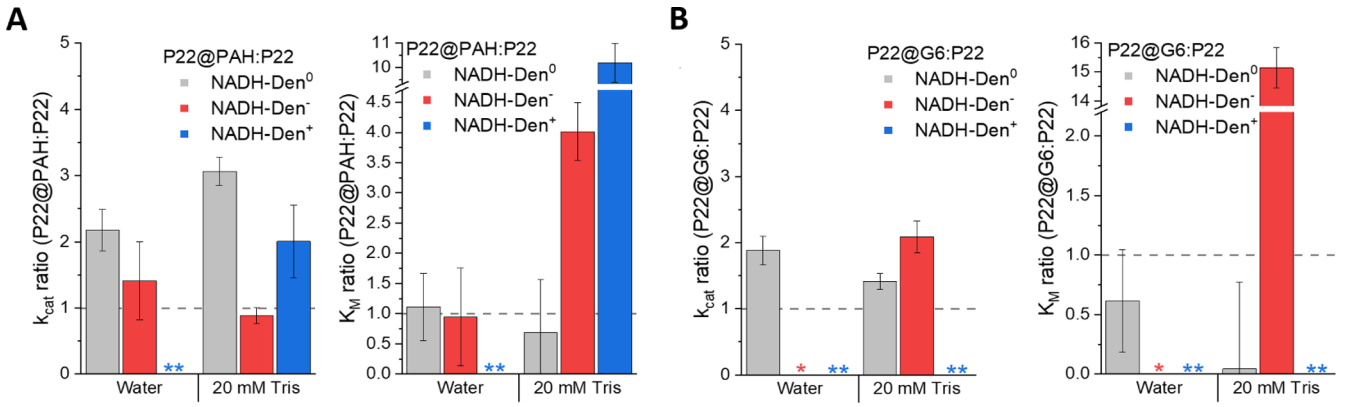

Figure 8. Michaelis−Menten kinetic constant ratios for NADH−Den oxidation by the P22@polymer. Asterisk (*) indicates that kinetic constants could not be calculated due to aggregation. Double asterisks (**) indicate that enzymatic activity could not be detected. (A) k_{cat} and K_M ratios for P22@PAH/P22 kinetic constants. (B) k_{cat} and K_M ratios for P22@G6/P22 kinetic constants.

are screened, leading to similar K_M values for oxidation of all three NADH−Den constructs by free AdhD−SP.

Effect of Polymer Coating on Encapsulated Enzyme Activity with Modified NADH Substrates. The assembled P22@polymer clusters responded slightly differently to the range of NADH−Den substrates, but overall the effect of the polymer coating on VLPs was less dominant on the behavior of the AdhD enzyme than the effects of encapsulation within the VLP. To illustrate the effects of the polymer coating on modified substrate behavior, we plot the ratio of k_{cat} for the P22@polymer/P22 (Figure 8).

The k_{cat} ratios for oxidation of NADH−Den^0 by P22@polymer show that the enzymatic activity is slightly higher than that for uncoated P22. The K_M ratios also do not change significantly. Together, this suggests that the coating of P22 with a polymer does not sterically inhibit the entry of even quite large molecules (approximately 6.8 kDa) into the capsid.

The k_{cat} ratio in 20 mM tris for NADH−Den$^-$ by both P22@G6 and P22@PAH suggests that there is no significant change in the catalytic activity of the enzyme. k_{cat} in water for P22@PAH also suggests little change, while kinetic constants could not be calculated for oxidation of NADH−Den$^-$ by P22@G6 in water because of aggregation, which interfered with absorbance readings. The aggregation behavior is likely the result of the strong attraction of the negatively charged NADH−Den$^-$ to exposed G6 on the P22 surface, a result of the charge-reversal on the nanoreactor. Because PAH is held more closely to the capsid and does not protrude from the capsid in the same way as the sterically bulky G6, aggregation of P22@PAH with NADH−Den$^-$ proceeds via the formation of smaller structures. As a result, the degree of scattering from aggregate formation between NADH−Den$^-$ and P22@PAH does not interfere with determination of kinetic constants, while the scattering from aggregation between P22@G6 and NADH−Den$^-$ obscures changes in the absorbance at 340 nm, preventing accurate determination of the change in the NADH concentration (Figure S20). The oxidation of NADH−Den$^-$ shows a high K_M ratio in 20 mM tris for both P22@PAH and P22@G6. The K_M ratio for P22@G6 is much higher than the K_M ratio for P22@PAH. The high K_M ratio for both materials indicates that the adsorbed polymer affects the uptake of NADH−Den$^-$ by P22, likely by inhibiting travel through the pore through electrostatic attraction of NADH−Den$^-$ to the positively charged polymer groups. The difference between the ratios for P22@PAH and P22@G6 may be the result of the geometry of the spherical dendrimer versus the linear polymer. Because the dendrimer is more sterically bulky, it may be more exposed when adsorbed to P22 and impede access to the pore more readily than the thin PAH chains.

Oxidation of NADH−Den$^+$ by P22@PAH in water proceeded with a high K_M ratio likely indicative of repulsive electrostatic interactions with the adsorbed PAH, which may work to counteract the effect of the electrostatic channel at the P22 pore. This indicates that the adsorbed polymer affects the uptake of highly charged substrates into the VLP. No kinetic constants were determined for the oxidation of NADH−Den$^+$ by P22@G6 in 20 mM tris due to significant aggregation, which interfered in absorbance readings. The lack of activity detected toward NADH−Den$^+$ in water is the result of inactivity of the enzyme toward this substrate, as mentioned previously.

The introduction of the charged polymer on P22 VLPs caused charge inversion on the VLP but still allowed access by some large, charged substrates to the enzyme inside. This means that the polymer localizes on P22 in a way that neutralizes much of the highly negatively charged groups on the capsid surface and inhibits the uptake of large, charged substrates, but still allows it to serve as a component of a hierarchically ordered enzyme material.

CONCLUSIONS

In this study, we have assembled VLP@polymer clusters through the introduction of cationic polymers to anionic P22 VLPs under low ionic strength conditions. The formation of small clusters aligned with simulations predicting the full coating of individual VLPs at low ionic strength. The P22@polymer clusters were larger than single-coated VLPs due to the mixing kinetics that allowed some bridging between particles to occur. Zeta potential measurements showed that the clusters exhibited charge reversal from their P22 building blocks. The VLPs incorporated an active enzyme encapsulated in their interior cavity, and the catalytic activity toward a small substrate molecules and large macromolecules was determined for each material and each component in the hierarchical assembly. We found that while the uptake of large, charged substrates was affected by both the polymer coating and encapsulation, the overall catalytic activity of the material was similar to that of its enzyme base. This allows us to control the charge on P22 nanoreactors without significant change to their catalytic ability, providing a path forward to further higher-

https://doi.org/10.1021/acs.biomac.1c00208
Biomacromolecules XXXX, XXX, XXX−XXX

order self-assembled materials with control over the catalytic functionality. The charge-inverse nature of the P22@polymer clusters changes their adsorption to charged surfaces, suggesting their suitability for use as a building block in further hierarchically ordered materials.

■ ASSOCIATED CONTENT

Supporting Information

The Supporting Information is available free of charge at https://pubs.acs.org/doi/10.1021/acs.biomac.1c00208.

Characterization data for P22 VLPs; characterization data for NADH-Den variants; DLS and zeta potential data for PAH, G6, and NADH−Den variants; kinetic data for NADH and NADH−Den oxidation; and zeta potential of polystyrene beads (PDF)

■ AUTHOR INFORMATION

Corresponding Author

Trevor Douglas − *Department of Chemistry, Indiana University, Bloomington 47405, Indiana, United States;* orcid.org/0000-0002-7882-2704; Email: trevdoug@indiana.edu

Authors

Pawel Kraj − *Department of Chemistry, Indiana University, Bloomington 47405, Indiana, United States*

Ekaterina Selivanovitch − *Department of Chemistry, Indiana University, Bloomington 47405, Indiana, United States*

Byeongdu Lee − *X-ray Science Division, Advanced Photon Source, Argonne National Laboratory, Argonne 60439, Illinois, United States;* orcid.org/0000-0003-2514-8805

Complete contact information is available at: https://pubs.acs.org/10.1021/acs.biomac.1c00208

Author Contributions

The manuscript was written through contributions of all authors. All authors have given approval to the final version of the manuscript.

Notes

The authors declare no competing financial interest.

■ ACKNOWLEDGMENTS

TEM images were collected at the Indiana University Electron Microscopy Center. DLS and zeta potential experiments were performed at the Indiana University Nanoscale Characterization Facility. SAXS data were collected at Beamline 12-ID-B, Advanced Photon Source, Argonne National Laboratory. PK was supported by a grant from the National Science Foundation through grant 1720625 and KS was supported by grant 4124801 from the Human Frontiers Science Program and the Graduate Training Program in Quantitative and Chemical Biology under Award T32 GM109825 and Indiana University. This research used resources of the Advanced Photon Source, a U.S. Department of Energy (DOE) Office of Science User Facility, operated for the DOE Office of Science by Argonne National Laboratory under Contract No. DE-AC02-06CH11357. Extraordinary facility operations were supported in part by the DOE Office of Science through the National Virtual Biotechnology Laboratory, a consortium of DOE national laboratories focused on the response to COVID-19, with funding provided by the Coronavirus CARES Act.

■ REFERENCES

(1) Park, C.; Raines, R. T. Quantitative Analysis of the Effect of Salt Concentration on Enzymatic Catalysis. *J. Am. Chem. Soc.* **2001**, *123*, 11472−11479.

(2) Liu, B.; Poolman, B.; Boersma, A. J. Ionic Strength Sensing in Living Cells. *ACS Chem. Biol.* **2017**, *12*, 2510−2514.

(3) Chen, H.; Meisburger, S. P.; Pabit, S. A.; Sutton, J. L.; Webb, W. W.; Pollack, L. Ionic strength-dependent persistence lengths of single-stranded RNA and DNA. *Proc. Natl. Acad. Sci. U.S.A.* **2012**, *109*, 799−804.

(4) Skolnick, J.; Fixman, M. Electrostatic Persistence Length of a Wormlike Polyelectrolyte. *Macromolecules* **1977**, *10*, 944−948.

(5) Decher, G.; Hong, J. D.; Schmitt, J. Buildup of ultrathin multilayer films by a self-assembly process: III. Consecutively alternating adsorption of anionic and cationic polyelectrolytes on charged surfaces. *Thin Solid Films* **1992**, *210−211*, 831−835.

(6) Lvov, Y.; Haas, H.; Decher, G.; Moehwald, H.; Mikhailov, A.; Mtchedlishvily, B.; Morgunova, E.; Vainshtein, B. Successive Deposition of Alternate Layers of Polyelectrolytes and a Charged Virus. *Langmuir* **1994**, *10*, 4232−4236.

(7) Caruso, F.; Trau, D.; Möhwald, H.; Renneberg, R. Enzyme Encapsulation in Layer-by-Layer Engineered Polymer Multilayer Capsules. *Langmuir* **2000**, *16*, 1485−1488.

(8) Sukhorukov, G. B.; Donath, E.; Lichtenfeld, H.; Knippel, E.; Knippel, M.; Budde, A.; Möhwald, H. Layer-by-layer self assembly of polyelectrolytes on colloidal particles. *Colloids Surf., A* **1998**, *137*, 253−266.

(9) Steinmetz, N. F.; Findlay, K. C.; Noel, T. R.; Parker, R.; Lomonossoff, G. P.; Evans, D. J. Layer-by-layer assembly of viral nanoparticles and polyelectrolytes: The film architecture is different for spheres versus rods. *ChemBioChem* **2008**, *9*, 1662−1670.

(10) Gu, H.; Dai, R.; Wei, Y.; Ji, H.-F. Functional layer-by-layer multilayer films for ion recognition. *Anal. Methods* **2013**, *5*, 3454.

(11) Uchida, M.; Klem, M. T.; Allen, M.; Suci, P.; Flenniken, M.; Gillitzer, E.; Varpness, Z.; Liepold, L. O.; Young, M.; Douglas, T. Biological containers: Protein cages as multifunctional nanoplatforms. *Adv. Mater.* **2007**, *19*, 1025−1042.

(12) Douglas, T.; Young, M. Viruses: Making friends with old foes. *Science* **2006**, *312*, 873−875.

(13) Ceres, P.; Zlotnick, A. Weak Protein−Protein Interactions Are Sufficient To Drive Assembly of Hepatitis B Virus Capsids†. *Biochemistry* **2002**, *41*, 11525−11531.

(14) Prevelige, P. E.; Thomas, D.; King, J. Scaffolding protein regulates the polymerization of P22 coat subunits into icosahedral shells in vitro. *J. Mol. Biol.* **1988**, *202*, 743−757.

(15) Sikkema, F. D.; Comellas-Aragonès, M.; Fokkink, R. G.; Verduin, B. J. M.; Cornelissen, J. J. L. M.; Nolte, R. J. M. Monodisperse polymer-virus hybrid nanoparticles. *Org. Biomol. Chem.* **2007**, *5*, 54−57.

(16) Chen, C.; Daniel, M.-C.; Quinkert, Z. T.; De, M.; Stein, B.; Bowman, V. D.; Chipman, P. R.; Rotello, V. M.; Kao, C. C.; Dragnea, B. Nanoparticle-Templated Assembly of Viral Protein Cages. *Nano Lett.* **2006**, *6*, 611−615.

(17) Selivanovitch, E.; Douglas, T. Virus capsid assembly across different length scales inspire the development of virus-based biomaterials. *Curr. Opin. Virol.* **2019**, *36*, 38−46.

(18) Tetter, S.; Hilvert, D. Enzyme Encapsulation by a Ferritin Cage. *Angew. Chem., Int. Ed.* **2017**, *56*, 14933−14936.

(19) Comellas-Aragonès, M.; Engelkamp, H.; Claessen, V. I.; Sommerdijk, N. A. J. M.; Rowan, A. E.; Christianen, P. C. M.; Maan, J. C.; Verduin, B. J. M.; Cornelissen, J. J. L. M.; Nolte, R. J. M. A virus-based single-enzyme nanoreactor. *Nat. Nanotechnol.* **2007**, *2*, 635−639.

(20) Edwards, E.; Roychoudhury, R.; Schwarz, B.; Jordan, P.; Lisher, J.; Uchida, M.; Douglas, T. Co-localization of catalysts within a protein cage leads to efficient photochemical NADH and/or hydrogen production. *J. Mater. Chem. B* **2016**, *4*, 5375−5384.

(21) Schwarz, B.; Madden, P.; Avera, J.; Gordon, B.; Larson, K.; Miettinen, H. M.; Uchida, M.; LaFrance, B.; Basu, G.; Rynda-Apple,

A.; Douglas, T. Symmetry Controlled, Genetic Presentation of Bioactive Proteins on the P22 Virus-like Particle Using an External Decoration Protein. *ACS Nano* **2015**, *9*, 9134−9147.
(22) Wen, A. M.; Steinmetz, N. F. Design of virus-based nanomaterials for medicine, biotechnology, and energy. *Chem. Soc. Rev.* **2016**, *45*, 4074−4126.
(23) Wen, A. M.; Lee, K. L.; Cao, P.; Pangilinan, K.; Carpenter, B. L.; Lam, P.; Veliz, F. A.; Ghiladi, R. A.; Advincula, R. C.; Steinmetz, N. F. Utilizing Viral Nanoparticle/Dendron Hybrid Conjugates in Photodynamic Therapy for Dual Delivery to Macrophages and Cancer Cells. *Bioconjugate Chem.* **2016**, *27*, 1227−1235.
(24) Kim, H.; Choi, H.; Bae, Y.; Kang, S. Development of target-tunable P22 VLP-based delivery nanoplatforms using bacterial superglue. *Biotechnol. Bioeng.* **2019**, *116*, 2843−2851.
(25) Lander, G. C.; Tang, L.; Casjens, S. R.; Gilcrease, E. B.; Prevelige, P.; Poliakov, A.; Potter, C. S.; Carragher, B.; Johnson, J. E. The structure of an infectious P22 virion shows the signal for headful DNA packaging. *Science* **2006**, *312*, 1791−1795.
(26) O'Neil, A.; Reichhardt, C.; Johnson, B.; Prevelige, P. E.; Douglas, T. Genetically Programmed In Vivo Packaging of Protein Cargo and Its Controlled Release from Bacteriophage P22. *Angew. Chem., Int. Ed.* **2011**, *50*, 7425−7428.
(27) Sánchez-Sánchez, L.; Tapia-Moreno, A.; Juarez-Moreno, K.; Patterson, D. P.; Cadena-Nava, R. D.; Douglas, T.; Vazquez-Duhalt, R. Design of a VLP-nanovehicle for CYP450 enzymatic activity delivery. *J. Nanobiotechnol.* **2015**, *13*, 66.
(28) Patterson, D. P.; Prevelige, P. E.; Douglas, T. Nanoreactors by Programmed Enzyme Encapsulation Inside the Capsid of the Bacteriophage P22. *ACS Nano* **2012**, *6*, 5000−5009.
(29) Kostiainen, M. A.; Hiekkataipale, P.; de la Torre, J. Á.; Nolte, R. J. M.; Cornelissen, J. J. L. M. Electrostatic self-assembly of virus-polymer complexes. *J. Mater. Chem.* **2011**, *21*, 2112−2117.
(30) Verwegen, M.; Cornelissen, J. J. L. M. Clustered Nanocarriers: The Effect of Size on the Clustering of CCMV Virus-Like Particles With Soft Macromolecules. *Macromol. Biosci.* **2015**, *15*, 98−110.
(31) Uchida, M.; McCoy, K.; Fukuto, M.; Yang, L.; Yoshimura, H.; Miettinen, H. M.; LaFrance, B.; Patterson, D. P.; Schwarz, B.; Karty, J. A.; Prevelige, P. E.; Lee, B.; Douglas, T. Modular Self-Assembly of Protein Cage Lattices for Multistep Catalysis. *ACS Nano* **2018**, *12*, 942−953.
(32) Aumiller, W. M., Jr.; Uchida, M.; Biner, D. W.; Miettinen, H. M.; Lee, B.; Douglas, T. Stimuli Responsive Hierarchical Assembly of P22 Virus-like Particles. *Chem. Mater.* **2018**, *30*, 2262−2273.
(33) Kostiainen, M. A.; Hiekkataipale, P.; Laiho, A.; Lemieux, V.; Seitsonen, J.; Ruokolainen, J.; Ceci, P. Electrostatic assembly of binary nanoparticle superlattices using protein cages. *Nat. Nanotechnol.* **2013**, *8*, 52−56.
(34) Velev, O. D. MATERIALS SCIENCE: Enhanced: Self-Assembly of Unusual Nanoparticle Crystals. *Science* **2006**, *312*, 376−377.
(35) Brunk, N. E.; Uchida, M.; Lee, B.; Fukuto, M.; Yang, L.; Douglas, T.; Jadhao, V. Linker-Mediated Assembly of Virus-Like Particles into Ordered Arrays via Electrostatic Control. *ACS Appl. Bio Mater.* **2019**, *2*, 2192−2201.
(36) Konarev, P. V.; Volkov, V. V.; Sokolova, A. V.; Koch, M. H. J.; Svergun, D. I. PRIMUS: a Windows PC-based system for small-angle scattering data analysis. *J. Appl. Crystallogr.* **2003**, *36*, 1277−1282.
(37) Jurrus, E.; Engel, D.; Star, K.; Monson, K.; Brandi, J.; Felberg, L. E.; Brookes, D. H.; Wilson, L.; Chen, J.; Liles, K.; Chun, M.; Li, P.; Gohara, D. W.; Dolinsky, T.; Konecny, R.; Koes, D. R.; Nielsen, J. E.; Head-Gordon, T.; Geng, W.; Krasny, R.; Wei, G.-W.; Holst, M. J.; McCammon, J. A.; Baker, N. A. Improvements to the APBS biomolecular solvation software suite. *Protein Sci.* **2018**, *27*, 112−128.
(38) Lee, C.-Y.; Kaplan, N. O. Characteristics of 8-substituted adenine nucleotide derivatives utilized in affinity chromatography. *Arch. Biochem. Biophys.* **1975**, *168*, 665−676.
(39) Kostiainen, M. A.; Kasyutich, O.; Cornelissen, J. J. L. M.; Nolte, R. J. M. Self-assembly and optically triggered disassembly of hierarchical dendron-virus complexes. *Nat. Chem.* **2010**, *2*, 394−399.
(40) Schönhoff, M. Layered polyelectrolyte complexes: physics of formation and molecular properties. *J. Phys.: Condens. Matter* **2003**, *15*, R1781−R1808.
(41) Jachimska, B.; Jasiński, T.; Warszyński, P.; Adamczyk, Z. Conformations of poly(allylamine hydrochloride) in electrolyte solutions: Experimental measurements and theoretical modeling. *Colloids Surf., A* **2010**, *355*, 7−15.
(42) Selivanovitch, E.; Lafrance, B.; Douglas, T. Molecular Exclusion Limits for Diffusion Across a Porous Capsid. *Nat. Commun.* **2021**, in press.
(43) Glasgow, J. E.; Asensio, M. A.; Jakobson, C. M.; Francis, M. B.; Tullman-Ercek, D. Influence of Electrostatics on Small Molecule Flux through a Protein Nanoreactor. *ACS Synth. Biol.* **2015**, *4*, 1011−1019.
(44) Llauró, A.; Luque, D.; Edwards, E.; Trus, B. L.; Avera, J.; Reguera, D.; Douglas, T.; de Pablo, P. J.; Castón, J. R. Cargo-shell and cargo-cargo couplings govern the mechanics of artificially loaded virus-derived cages. *Nanoscale* **2016**, *8*, 9328−9336.
(45) Solanki, K.; Abdallah, W.; Banta, S. Extreme makeover: Engineering the activity of a thermostable alcohol dehydrogenase (AdhD) fromPyrococcus furiosus. *Biotechnol. J.* **2016**, *11*, 1483−1497.

https://doi.org/10.1021/acs.biomac.1c00208
Biomacromolecules XXXX, XXX, XXX−XXX